Monitoring the Sky Conditions at Skinakas Observatory: I. The moonless Night Sky Brightness

Makis Palaiologou

University of Crete, Department of Physics, Voutes University Campus, GR-70013 Heraklion, Greece

In an attempt to quantify the sky quality at Skinakas Observatory, I had performed and analyzed all-sky photometric observations back in August 2008. Since then, the need to re-evaluate the artificial light pollution impact on the site emerged strongly, as visual inspection suggested a substantial increase of the nighttime outdoor lighting, especially during the summer and autumn seasons, in the island of Crete.

The 2016 photometric campaign

During observation planning and scheduling, in order to achieve the best possible uniformity in telescope pointings in altitude-azimuth, the observable part of the celestial sphere was divided in 25 Areas of equal solid angle (Fig. 1), with respect to the local horizontal coordinate system. The basic idea was to observe exclusively standard star fields from the catalogs of A. Landolt (1992; 2013) and P. Stetson (`https://www3.cadc-ccda.hia-iha.nrc-cnrc.gc.ca/en/community/STETSON/index.html`).

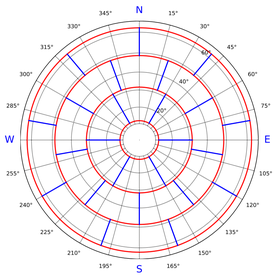

Figure 1. The division of the celestial cap (airmass $\lesssim$ 2.2) into **Zones** (the spherical segments confined between the constant-altitude red circles) and the **Areas** in each Zone (bounded by the blue constant-azimuth lines).

Care has been taken to exclude fields with Galactic latitude $|b| < 15°$, but no constraint was applied to their ecliptic coordinates. Also, to minimize the contribution of moonlight and zodiacal radiation, the observing time window limits were chosen to be at least 30 min away from the respective twilight and Moon altitude lower than $-5°$. The schedule of observations included targets covering a wide range of airmasses, along with alternative fields to handle possible cancellations imposed by weather conditions (e.g. strong wind direction). The ultimate goal would be to observe standard fields through each Area at least 3 times during the whole run.

Observations and data reduction

The actual observations were held in 12 nights, spread over a period from early June to late October 2016 (6 and 5 June; 1–3, 5 July; 28–30 September; 1, 2 and 29 October), using the 1.29 m (f/7.6) Ritchey–Chrétien telescope at Skinakas Observatory. A total of 586 images were acquired with a 2048 × 2048 back-illuminated, deep-depletion CCD camera (Andor iKon-L) with pixel size 13.5 μm. The system provided a $9\farcm6 \times 9\farcm6$ field of view and image scale $0\farcs28$ per pixel. Standard broadband BVR Johnson-Cousins filters were used and typical exposure times were 240s, 180s and 150s in B, V and R filters, respectively. The sequence of exposures taken in each fields was either BVRRVBBVR or RVBBVRRVB. Several bias and twilight sky flats were also obtained on a daily basis. The raw images were reduced using IRAF software procedures for bias subtraction and flat-field correction. Dark-current subtraction was not necessary, because it is negligibly small.

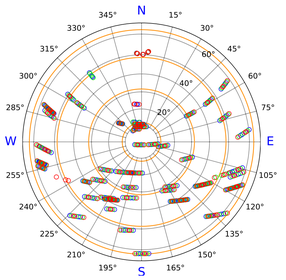

Figure 2. The actual telescope pointings of the acquired images. The colored symbols correspond to the filter used: Blue for B filter, green for V and red for the R filter images.

As seen in Fig. 2, there is a noticeable asymmetry between the N-S sky coverage. Since the prevailing wind direction at the Skinakas plateau is NW to N, and as roughly 40% of the observing time was affected by relatively strong wind, we were forced to skip some of the Northern targets and replace them by Southern ones.

Photometric analysis

Image calibration was followed by aperture photometry (DAOPHOT, Stetson, 1987) growth curve correction (DAOGROW, Stetson, 1990) and standard star identification in each image. Transformation equations, connecting instrumental to absolute magnitudes (in the Landolt system), were solved for each night's data, and are of the form:

$$\begin{aligned} b_{fi} &= \zeta_{b,f} + B_i + \alpha_b\,(B_i - V_i) + \beta_b\,(B_i - V_i)^2 \\ v_{fi} &= \zeta_{v,f} + V_i + \alpha_v\,(B_i - V_i) + \beta_v\,(B_i - V_i)^2 \\ r_{fi} &= \zeta_{r,f} + R_i + \alpha_r\,(V_i - R_i) + \beta_r\,(V_i - R_i)^2 \end{aligned} \quad (1)$$

where small letters (b, v, r) correspond to instrumental magnitudes and capitals (B, V, R) denote the absolute magnitudes in the corresponding filters. Subscript f stands for an individual frame (image) and subscript i is a counter index for all standard stars in image f. The color coefficients α and β are kept at the same (but yet unknown) value for all images taken during the night, for each filter. On the other hand, the ζ terms – which, actually, are the sum of the photometric zero-point and the atmospheric extinction terms – are free to change for each image. The unknown coefficients were determined by robust weighted least squares.

Next, all ζ terms were decomposed into a zero-point term (z) and the atmospheric extinction contribution, as given in Eq. 2, with the same meaning of f as before. k denotes the extinction coefficient (in magnitudes per airmass) and X_f the airmass of the observed frame f. Thus, the extinction coefficient is common among all frames taken in the night, but the photometric zero-points may vary between frames.

$$\begin{aligned} \zeta_{b,f} &= z_{b,f} + k_b\,X_f \\ \zeta_{v,f} &= z_{v,f} + k_v\,X_f \\ \zeta_{r,f} &= z_{r,f} + k_r\,X_f \end{aligned} \quad (2)$$

Again, the parameters in Eq. 2 are found through least squares fit.

Finally, the sky background I_{sky} was estimated, during the aperture photometry calculation, within an annulus of inner and outer radii of 20 and 40 pixels, respectively. The instrumental sky brightness m_{sky}, expressed in mag arcsec^{-2}, is given by

$$m_{sky} = -2.5\,log(\frac{I_{sky}}{t_{exp}\,p^2}), \quad \text{and error} \quad \sigma(m_{sky}) = 1.0857\,\frac{\sigma(I_{sky})}{I_{sky}}$$

with p the detector pixel scale (arcsec pix^{-1}) and t_{exp} the exposure time in seconds. The photometrically calibrated sky magnitude is obtained by

$$M_{sky} = m_{sky} - m_* + M_* + k\,X_* + \alpha\,(C_* - C_{sky}) + \beta\,(C_* - C_{sky})^2 \quad (3)$$

where M_{sky}, m_{sky} the calibrated and instrumental sky magnitudes (in mag arcsec^{-2}), M_*, m_* the corresponding values for a standard star observed at airmass X_*; k, α, β are the extinction and color coefficients and C_{sky}, C_* the colors of the sky and standard star, respectively. As the sky colors are not known in advance, an iterative procedure was applied to Eq. 3 for each filter, to recover these values on a night-by-night basis. The sky colors converged not far from the starting values used, $(B-V)_{sky} = 1.0$ and $(V-R)_{sky} = 0.9$.

Following common practice (e.g. Pilachowski et al., 1989; Krisciunas & Schaefer, 1991; Patat, 2003), the sky surface brightness is calibrated with no correction for atmospheric extinction, since the major source of night sky emission is the airglow, taking place in the atmosphere itself. However, in order to compare or combine together sky brightness values obtained at different airmasses, one needs to take into account the fact that sky becomes inherently brighter for increasing zenith distances (Patat, 2003, and references therein). Therefore, we applied a zenith correction to the sky surface magnitudes, to compensate for this effect, following the prescription developed by Patat (2003, appendix C). Thus, denoting by f the fraction of the total sky brightness due to the airglow emission, then the remaining $1 - f$ part represents the contribution to the sky background from sources beyond the atmosphere, such as zodiacal light, faint starlight and deem galaxies. The zenith–corrected sky magnitude is given by

$$M_{sky,ZC} = M_{sky} + 2.5\,log(1 - f + f\,X) + k\,(1 - X)$$

We used $f = 0.6$, as suggested by Garstang (1989, Eq. 29)

Results

Zenith corrected magnitudes are shown in Fig. 3 as a function of airmass and azimuth (measured from North to East in degrees) for all 3 filters used. Fig. 4 depicts the weighted mean value calculated in groups of azimuth sectors (left) and altitude zones (right panel) along with the Zenith average.

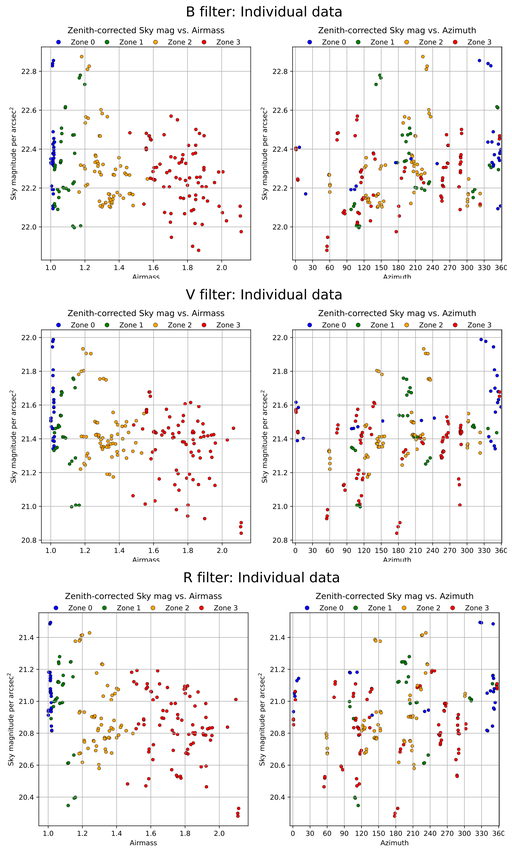

Figure 3. Zenith-corrected absolute sky magnitudes as a function of airmass (*left column frames*) and versus the azimuth (*right column*) of the observed field, through B, V and R filters. Each marker's color corresponds to telescope pointing at a different altitude zone (see legend above each frame).

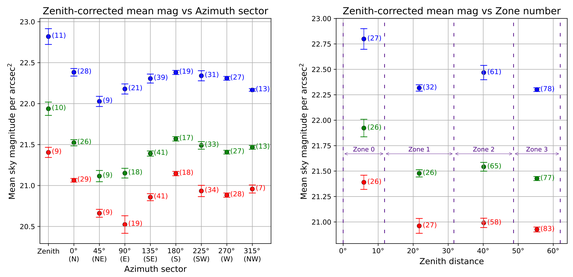

Figure 4. *Left panel.* Zenith-corrected absolute sky magnitudes averaged over 8 azimuthal spherical sectors, centered at 8 principal azimuth directions and width 45°, along with the Zenithal-cap (Zone 0) area. The color of the markers indicate the filter used for the sky magnitude. Numerals in parentheses correspond to the number of images used to derive the weighted mean value.
Right frame. Same as the left panel plot, but here the averages are computed in horizontal sectors (bounded by constant altitude circles), with the same color-code for the points and meaning of the numbers next to them.

All sky maps

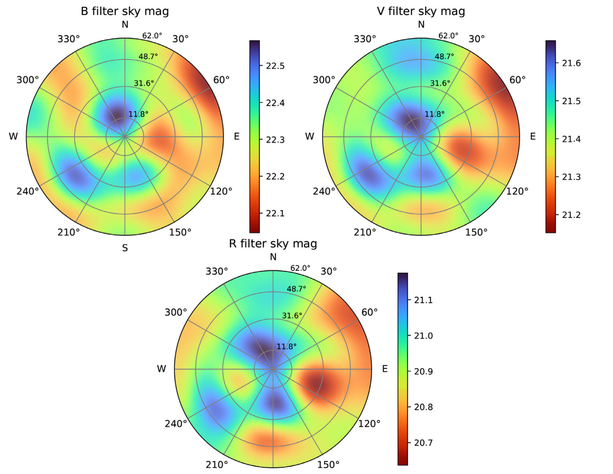

Figure 5. Zenith-corrected night sky surface brightness maps in the passband of B, V and R filters, expressed in magnitudes arcsecond^{-2}. The polar grid indicates the local horizontal coordinate system, with constant zenith-distance circles corresponding to the lower boundary of the 4 Zones considered.

Solar activity index

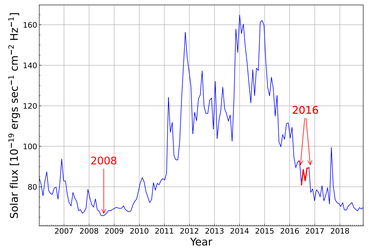

Figure 6. 10.7 cm solar flux activity index during Solar Cycle 24. The red arrows indicate the time periods sky brightness data were obtained. Flux values are averages over a complete solar rotation (roughly 27 days), based on data from the Solar Radio Monitoring Program, a service operated by the National Research Council and Natural Resources Canada.

Comparing results between 2008 and 2016

	B mag		V mag		R mag	
Year	Zenith	All-sky	Zenith	All-sky	Zenith	All-sky
2008	22.51 ± 0.05	22.36 ± 0.16	21.74 ± 0.06	21.60 ± 0.14	21.18 ± 0.07	21.07 ± 0.14
2016	22.80 ± 0.10	22.35 ± 0.03	21.92 ± 0.09	21.50 ± 0.02	21.39 ± 0.07	20.98 ± 0.04

There is no strong evidence for significant differences.

References

Garstang, R. H. 1989, PASP, 101, 306
Krisciunas, K. & Schaefer, B. E. 1991, PASP, 103, 1033
Landolt, A. U. 1992, AJ, 104, 340
Landolt, A. U. 2013, AJ, 146, 131
Patat, F. 2003, A&A, 400, 1183
Pilachowski, C. A., Africano, J. L., Goodrich, B. D., & Binkert, W. S. 1989, PASP, 101, 707
Stetson, P. B. 1987, PASP, 99, 191
Stetson, P. B. 1990, PASP, 102, 932